

Machine-learning-assisted Blending of Data-Driven Turbulence Models

Mourad Oulghelou^{1,2*†}, Soufiane Cherroud^{3†}, Xavier Merle³,
Paola Cinnella¹

¹*Institut Jean Le Rond D'Alembert, Sorbonne Université,
4 Place Jussieu, Paris, 75005, France.

²Computing and Data Science Institute, Sorbonne Université,
4 Place Jussieu, Paris, 75005, France.

³DynFluid Laboratory, Arts et Métiers Institute of Technology,
155 bd. de l'Hôpital, Paris, 75013, France.

*Corresponding author(s). E-mail(s):

mourad.oulghelou@sorbonne-universite.fr;

Contributing authors: soufiane.cherroud@ensam.eu;

xavier.merle@ensam.eu; paola.cinnella@sorbonne-universite.fr;

[†]These authors contributed equally to this work.

Abstract

A machine learning-based methodology for blending data-driven turbulent closures for the Reynolds-Averaged Navier-Stokes (RANS) equations is proposed to improve the generalizability across different flow scenarios. Data-driven models based on sparse Bayesian learning and symbolic regression are pre-trained for specific flow classes, including turbulent channel flows, separated flows, and axisymmetric jets. The specialized models (called "*experts*") are then blended using a set of weighting functions that reflect the local likelihood of a model to capture the reference data. The weighting functions are expressed as functions of a set of local flow features, and Random Forest regressors (RFR) are trained alongside the expert models to learn the mapping between the features and the weights. The training dataset includes additional data for flows ranging from shear flows at equilibrium to separated flows. The resulting blended model is then used to predict unseen flows, including a turbulent zero-pressure-gradient flat plate and a wall-mounted hump involving attached and separated boundary layer regions. The results show that the blending strategy adapts to the

local flow conditions and effectively leverages the strengths of individual models, promoting the best-performing models locally, in a manner consistent with the training scenarios. The blended model provides a robust approximation for unseen flows that exhibit similar underlying physical characteristics to the training cases, while also successfully extrapolating to flows with different geometries and physical configurations.

Keywords: Data-driven models, Symbolic Regression, Model mixtures, turbulence models

1 Introduction

Turbulence models are a crucial component of Computational Fluid Dynamics (CFD) solvers for engineering applications, which mostly rely on the Reynolds-Averaged Navier-Stokes (RANS) equations. Most modeling efforts target unclosed terms, known as Reynolds Stresses, which represent the contribution of the unresolved turbulent scales to the transport of mean flow momentum. Although a considerable number of models have been developed with varying degrees of success in predicting flows (see [1–5] for overviews), none has been shown to be systematically superior or hopeless [1], and turbulence modeling continues to be an active area of research [6]. Most RANS turbulence models are known to face challenges with complex flows involving turbulence nonequilibrium, strong gradients, separations, shocks, and 3D effects. The shortcomings are particularly significant for the so-called linear eddy viscosity models (LEVM), which rely on Boussinesq’s hypothesis of a linear relationship between the turbulent stresses and the mean flow deformation [3, 7]. Despite their limitations, LEVM remain the most widely used turbulence models in industrial flow solvers because of their good tradeoff between accuracy, computational cost, and robustness. Efforts to enhance LEVM include rotation corrections [8], non-linear models [9], elliptic relaxation models [10], algebraic and explicit algebraic Reynolds Stress models [11–14], and full Reynolds Stress Models [15]. However, most of these more sophisticated models have had limited success in CFD applications due to their higher cost and lower robustness; they also involve numerous adjustable coefficients, often calibrated against a limited set of so-called ”canonical flows”, which correspond to simplified turbulence states that, while occurring in subregions of more general flows, are not fully representative of the flow behavior in complex configurations. Overall, the variety of model formulations and associated closure coefficients represent a significant source of uncertainty in flow simulations [16].

Over the past decade, Machine Learning (ML) has emerged as an attractive option for enhancing turbulence models by relaxing some of the simplifying modeling assumptions and by leveraging the information contained in high-fidelity data sets [16–19]. Various flavors of ML-supported turbulence models have been proposed, most of which consist of learning some form of correction terms from the data to improve the representation of the Reynolds Stresses, the auxiliary equations used to describe the evolution of turbulent scales, or both. The corrections are generally learned for

specific flow classes, e.g. separated flows [20–24], airfoils [25, 26], wind turbine wakes [27], secondary flows [28] and, more rarely, on several flows simultaneously [29, 30]. While data-driven models learned on narrow flow classes can significantly improve accuracy over baseline models, they do not generalize to radically different flows, and often deteriorate the representation of canonical flows for which the baseline models were calibrated. On the other hand, multi-flow learning may lead to a soft compromise solution, thus limiting potential improvements over standard models [31]. Enriching the set of features used to represent the data-driven corrections help improving generalizability but, even so, separated models are needed to accurately represent flows involving different physical processes, i.e. free-shear or wall-bounded flows. In addition to multi-flow training, so-called progressive augmentation techniques [32], consisting in learning corrective terms for specific flow classes (e.g. separated flows [33] or secondary flows [34]) while preserving the attached boundary layer representation, have been shown able to capture a wider set of flows. However, complex flows involving various processes simultaneously (e.g. separation and secondary flows) may still require the introduction of thresholding functions to activate or deactivate each correction as required.

An attractive alternative is represented by so-called mixture models [35–39], which consist in blending together the predictions of a set of competing models. Initially introduced for quantifying model-form uncertainties (i.e. uncertainties associated with the model mathematical structure) [40–42]), they also offer promise for improving the model predictive performance by promoting (downgrading) the component models in the mixture in the regions where they perform the worst.

Previous work by some of the present authors showed the potential of adopting mixture-of-expert approaches [43, 44] in turbulence modeling [36, 37]. Similarly to Bayesian model averaging techniques [45], a convex linear combination of the component model outputs is used to estimate the posterior probability distribution of some quantity of interest (QoI). The combination coefficients are trained to assign to the models high weights in regions where they best perform, and low ones in regions of high inaccuracy. Such regions are identified through a set of local flow features, so that the local weights are learned under the form of input/output relationships between the input features and the weights. While such "external" or "non-intrusive" mixtures of turbulence model solutions have been shown to accurately capture a diversity of flows not seen at training [36, 37], the aggregated solution is not a solution of the governing equations, and may violate conservation principles to some extent. Furthermore, similarly to other uncertainty quantification approaches, external model mixtures require predicting a new flow with each component model before aggregating the results. If N_M models are used, the prediction cost amounts to that of N_M simulations.

On the other hand some authors have proposed an internal blending of models. For instance, [35] and [38] have proposed training classifiers alongside data-driven models, to recognize regions where the flow is similar to the conditions seen at training. Ref. [39] has proposed an internal model mixture using the posterior variances of stochastic data-driven models (represented as Gaussian processes) to build the weights. In

this work, we build of the space-dependent model aggregation (XMA) approach initially proposed in [36], and further developed in [37], and we propose a strategy for blending a set of flow-specific data-driven turbulence model corrections, or "experts", using weighting functions trained across several flow cases. The blended data-driven corrections are then applied to a baseline model and propagated through the RANS equations, to predict the QoIs. Because the predictions are solutions to the RANS equations under the blended data-driven model, they satisfy the conservation properties. Additionally, a single simulation is now necessary to formulate predictions. As a downside, the information about the predictive uncertainty is lost.

The remainder of this paper is organized as follows. In Section 2, we recall the data-driven framework used to train expert models for selected flow classes. Section 3 introduces the proposed blending strategy and the methodology used to learn the model weighting functions. In Section 4, we present and discuss the results for training and test turbulent flow scenarios, highlighting the improvements in predictive accuracy and physical fidelity. Finally, in Section 5, we draw conclusions and outline potential avenues for future research.

2 Data-driven augmentation of RANS models

We investigate data-driven turbulence models supplementing the incompressible RANS equations for a constant-property fluid, written as:

$$\begin{cases} \partial_i U_i &= 0, \\ U_j \partial_j U_i &= \partial_j \left[-\frac{1}{\rho} P + \nu \partial_j U_i - \tau_{ij} \right], \end{cases}$$

where U_i is the mean velocity, ρ is the constant density, P is the mean pressure and ν is the constant kinematic viscosity. The Reynolds-stress τ_{ij} is the target of modelling. This symmetric, positive semi-definite, second-order tensor can be decomposed into an anisotropic $a_{ij} = 2kb_{ij}$ and an isotropic part $\frac{2}{3}k\delta_{ij}$

$$\tau_{ij} = 2k \left(b_{ij} + \frac{1}{3}\delta_{ij} \right), \quad (1)$$

where k is the turbulent kinetic energy and δ_{ij} the Kroenecker symbol. In the baseline model, the non-dimensional anisotropy tensor b_{ij} is represented as a linear function of the mean-strain rate tensor $S_{ij} = \frac{1}{2} \left(\frac{\partial U_i}{\partial x_j} + \frac{\partial U_j}{\partial x_i} \right)$ via the scalar eddy viscosity ν_t :

$$b_{ij} \approx b_{ij}^0 = -\frac{\nu_t}{k} S_{ij}$$

which is known to be a rather simplistic representation of the physical reality (see e.g. [3]). Furthermore, additional modeling assumptions are used to relate ν_t to the mean flow variables and turbulent properties. In the k - ω SST model [46], ν_t is computed using two auxiliary transport equations for k and for the specific dissipation

rate ω . Both equations contain several unclosed terms that are generally modeled on the ground of dimensional considerations and empirical closure coefficients. As a consequence, the modeled turbulent kinetic energy budget differs from the exact one, e.g. obtained from a well-resolved DNS, and this leads to significant discrepancies between the turbulent scales derived from the modeled k and ω and the exact ones. Hereafter, we follow the approach initially proposed in [21], and we augment the baseline constitutive relation by adding a corrective term b_{ij}^Δ :

$$b_{ij} = b_{ij}^0 + b_{ij}^\Delta. \quad (2)$$

This additive correction, leaving the linear term unaltered, has the benefit of enhanced numerical stability [47]. Furthermore, we also augment the k - ω transport equations to account for modeling discrepancies with the exact turbulent kinetic energy equation. Finally, the augmented transport equations are:

$$U_j \partial_j k = P_k + R_k - \beta^* \omega k + \partial_j [D_k^{\text{Eff}} \partial_j k], \quad (3)$$

$$U_j \partial_j \omega = \gamma(\tilde{P}_k + R_k) - \beta \omega^2 + \partial_j [D_\omega^{\text{Eff}} \partial_j \omega] + CD_{k\omega}, \quad (4)$$

where

$$\begin{aligned} P_k &= \min \left\{ 2(\nu_t S_{ij} - k b_{ij}^\Delta) \partial_j U_i; c_1 \beta^* k \omega \right\}, \\ \tilde{P}_k &= \min \left\{ 2(S_{ij} - \frac{k}{\nu_t} b_{ij}^\Delta) \partial_j U_i; \frac{c_1}{a_1} \beta^* \omega \max\{a_1 \omega; b_1 F_2 \sqrt{S}\} \right\}, \\ CD_{k\omega} &= 2\alpha_\omega \frac{1}{\omega} (\partial_i k) (\partial_i \omega), \end{aligned} \quad (5)$$

and the remaining auxiliary equations and parameters of k - ω SST model are given in Appendix B. Given k and ω , the eddy viscosity ν_t is updated as follows

$$\nu_t = \frac{a_1 k}{\max(a_1 \omega, \sqrt{S} F_{23})}, \quad \text{with } S = 2S_{ij} S_{ij} \quad (6)$$

It is important to note that in the augmented transport equations (3) and (4), a residual correction term R_k is introduced. This term serves as a correction to the modified production term augmented by the extra anisotropy tensor b_{ij}^Δ . In the following, a strategy to calculate the correction terms b_{ij}^Δ and R_k is detailed.

2.1 Target corrective fields

To proceed with the data-driven augmentation, both *a priori* or *a posteriori* training can be adopted. In the former, the full corrective fields b_{ij}^Δ and R_k are first derived from high-fidelity simulations or experiments, and then used as the training target. The resulting data-driven corrections are then added to the baseline model and propagated through the flow solver. Such an approach has the merit of low cost and ease

of training, but it can lead to inconsistencies between the training and the prediction environment, where the modeled quantities are used as the model inputs instead of the high-fidelity ones seen at training. Such inconsistency can be mitigated by using *a posteriori* or *model-consistent* training [48], but at the cost of solving an expensive high-dimensional optimization problem [49]. In the following, we only consider data-driven corrections learned via *a priori* training.

To reduce the model inconsistency, which is mostly related to the discrepancy between the exact and modeled turbulent scales, we adopt the *k*-corrective frozen RANS procedure from [21] to derive the target fields b_{ij}^Δ and R_k from a set of high-fidelity data. The latter is an iterative approach consisting in passively solving the turbulence transport equation under high-fidelity mean-velocity and turbulent kinetic energy fields. This delivers estimates of the specific dissipation ω and extra production R_k model suitable to match the exact kinetic energy equation.

The procedure begins with an initial guess of the eddy viscosity ν_t derived from an initial or randomized ω . The extra anisotropy term b_{ij}^Δ is evaluated as:

$$b_{ij}^\Delta = \frac{\nu_t}{k} S_{ij} + b_{ij}, \quad (7)$$

and then injected into the turbulent kinetic energy transport equation to determine the residual R_k :

$$R_k = U_j \partial_j k - P_k + \beta^* \omega k - \partial_j [D_k^{\text{Eff}} \partial_j k], \quad (8)$$

By substituting the obtained residual into the specific dissipation rate equation (4), a solution for ω can be found, and the "high-fidelity" eddy viscosity is updated using (6). By iterating this process and refining ω at each step until convergence, the corrected augmented model with the obtained b_{ij}^Δ and R_k will converge to a solution that more accurately approaches the high-fidelity turbulent flow's solution.

2.2 Data-driven models

Modeling ansatzs for the corrective terms b_{ij}^Δ and R_k are obtained as in [23] by projecting them onto an invariant tensor basis. Specifically, the extra anisotropic tensor b_{ij}^Δ is projected onto the minimal integrity bases initially proposed in [12] and reformulated in [13]:

$$b_{ij}^\Delta = \sum_{n=1}^{10} \alpha_n^\Delta(I_1, \dots, I_5) T_{ij}^{(n)}(S_{ij}^*, \Omega_{ij}^*), \quad (9)$$

where $T_{ij}^{(n)}$ are the tensor basis functions built from the non-dimensional strain and rotation rates (S_{ij}^* and Ω_{ij}^* , respectively), and the functions α_n depend on a set of associated invariants I_1, \dots, I_5 . For the two-dimensional flows of interest here, only three of these tensor basis functions and two invariants are needed:

$$T_{ij}^{(1)} = S_{ij}^*, \quad I_1 = S_{mn}^* S_{nm}^*,$$

$$\begin{aligned}
T_{ij}^{(2)} &= S_{ik}^* \Omega_{kj}^* - \Omega_{ik}^* S_{kj}^*, & I_2 &= \Omega_{mn}^* \Omega_{nm}^*, \\
T_{ij}^{(3)} &= S_{ik}^* S_{kj}^* - \frac{1}{3} \delta_{ij} S_{mn}^* S_{nm}^*,
\end{aligned}$$

with $S_{ij}^* = \frac{S_{ij}}{\omega}$, $\Omega_{ij}^* = \frac{\Omega_{ij}}{\omega}$ and $\Omega_{ij} = \frac{1}{2} (\partial_j U_i - \partial_i U_j)$. Then, the extra anisotropy correction tensor reduces to:

$$b_{ij}^\Delta = \sum_{n=1}^3 \alpha_n^\Delta(I_1, I_2) T_{ij}^{(n)}(S_{ij}^*, \Omega_{ij}^*). \quad (10)$$

Following [21] and [23], the scalar correction term R_k is expressed as a "production-like" term, modeled as the inner product of a second-order symmetric tensor b_{ij}^R and the mean velocity gradient (see [50] for an alternative, "dissipation-like" formulation):

$$R_k = 2k b_{ij}^R \partial_j U_i, \quad (11)$$

where b_{ij}^R is represented with the same tensor basis as b_{ij}^Δ

$$b_{ij}^R = \sum_{n=1}^3 \alpha_n^R(I_1, I_2) T_{ij}^{(n)}(S_{ij}^*, \Omega_{ij}^*). \quad (12)$$

Using the preceding representations, the modeling target is now represented by the functions $\alpha_n^{\Delta, R}$.

The α_n^Δ and α_n^R are learned from data by means of a symbolic regression algorithm. Specifically, we use a Sparse Bayesian Learning (SBL) algorithm, originally proposed in [51], for the Sparse Regression of Turbulent stress Anisotropy (SpaRTA), used in [23] to regress the α functions from a large dictionary of monomials of the invariants I_1 and I_2 . The reader is referred to [23] for details about the algorithm.

In [37], SBL-SpaRTA has been used to train data-driven corrections of the k - ω SST for various flow cases, including turbulent channel flows, zero-pressure-gradient and adverse-pressure-gradient boundary layers, an axisymmetric near-sonic jet, and separated flows. As an outcome, sparse symbolic models have been identified whose parameters are endowed with Gaussian posterior probability distributions. Such models have been shown to outperform the other models for flows similar to those used for their training, but to be inaccurate when applied to flows significantly different from those in their training sets. For instance, the separated flow model and jet model, do not predict correctly the law of the wall for attached wall-bounded flows; conversely, the attached-flow models perform poorly for separated flows or jets. Notably, models for channel flows and boundary layers are found to be quite similar and relatively close to the baseline. For this reason, in [37] a model aggregation method has been proposed to account for the uncertainty introduced by data-driven RANS models for complex flows involving several physical processes simultaneously (in particular,

Models	Data-driven corrections	Training cases
M_{SST}	$b^\Delta = [0]$ $b_R^\Delta = [0]$	Baseline $k - \omega$ SST
M_{ANSJ}	$b^\Delta = [(0.25 \pm 7.26 \cdot 10^{-3})] T^{(1)}$ $b_R^\Delta = [0] \pm 6.55 \cdot 10^{-5}$	PIV of near sonic axisymmetric jet [53]
M_{SEP}	$b^\Delta = [(5.21 \pm 0.0173)] T^{(2)}$ $b_R^\Delta = [(0.681 \pm 0.02)] T^{(1)}$	LES of periodic-hills (PH) at $Re = 10595$ [54, 55] DNS of converging-diverging (CD) at $Re = 13600$ [56] LES of curved backward-facing step (CBFS) at $Re = 13700$ [57]

Table 1: Experts selected for model aggregation.

attached boundary layers, separation, and free shear).

Hereafter, we follow a similar idea to generate a more universal data-driven model by blending together various data-driven models. For simplicity, we consider only three "expert" models in the following of the study, namely, the baseline model (denoted M_{SST}), which is selected as the "expert" for attached wall-bounded flows, and the expert models for separated flows and jets, noted M_{SEP} and M_{ANSJ} . The expression of these three models, alongside the sources of the data used for their training, are given in Table 1. More details about model training can be found in [37]. In the table, the data-driven model parameters are reported with the corresponding standard deviations, since SBL-SpaRTA delivers stochastic models endowed with posterior probability distributions. Given the posterior model variances are small compared to the mean, the model parameters will be treated as deterministic in the following to simplify the presentation. However, it is also possible to apply the proposed aggregation methodology to models with parametric uncertainties, see [52] for more details.

3 Machine-learning-based model blending

To overcome the limitations of individual expert models and promote generality, we introduce a blending strategy based on the space-dependent aggregation of a set of expert data-driven model corrections, namely $\mathcal{M} = \{M_{\text{SST}}, M_{\text{SEP}}, M_{\text{ANSJ}}\}$. The blended model is denoted M_{blend} . The corrective tensors b_{ij}^Δ and b_{ij}^R are written as a linear convex combination of the expert corrections, using a data-driven set of weighting functions w_M .

$$b_{ij}^\Delta = \sum_{M \in \mathcal{M}} w_M b_{ij}^{\Delta, M}, \quad b_{ij}^R = \sum_{M \in \mathcal{M}} w_M b_{ij}^{R, M} \quad (13)$$

with $\sum_{M \in \mathcal{M}} w_M = 1$. The weighting functions are designed to dynamically adjust in space, based on a set of local flow features, so to assign high weights to the experts that are most likely to perform accurately based on the local flow conditions, and low weights to the unsuitable ones. Following [37], we adopt a set of eleven features derived

from [58], noted $\boldsymbol{\eta}(\mathbf{x}) = (\eta_1(\mathbf{x}), \dots, \eta_{11}(\mathbf{x}))$ and described in the Appendix A, which have been widely used in the literature to represent data-driven corrections. Second, we define the exact model weights as:

$$\omega_L = \frac{\mathcal{G}(\delta^L, \bar{\delta})}{\sum_{M \in \mathcal{M}} \mathcal{G}(\delta^M, \bar{\delta})}$$

where \mathcal{G} is a function that depends on the model outputs for some observed QoI $\{\delta^M\}_{M \in \mathcal{M}}$, and on the corresponding ground truth values $\bar{\delta}$, extracted from a high-fidelity database. Note that by construction the weights ω_L sum up to 1. We chose \mathcal{G} to be the Gaussian kernel, given for $\sigma > 0$ by

$$\mathcal{G}(\delta^L, \bar{\delta}) = \exp\left(-\frac{\|\delta^L - \bar{\delta}\|^2}{2\sigma^2}\right) \quad (14)$$

The function \mathcal{G} assigns higher weights to models that are closer to the ground truth data $\bar{\delta}$ and lower weights to those that are farther away. The bandwidth parameter σ controls how fast the weight decreases with increasing errors, and it is sought from a set of user-defined values $\mathcal{E} = \{1, 10^{-1}, 10^{-2}, 10^{-3}, 10^{-4}\}$ using a grid search method. The optimal choice of σ is based on the minimal distance between high-fidelity QoI and the average expert model output based on the Gaussian weights w_M , i.e.,

$$\sigma_{opt} = \underset{\sigma \in \mathcal{E}}{\operatorname{argmin}} \left\| \left(\sum_{M \in \mathcal{M}} w_M(\sigma) \delta^M \right) - \bar{\delta} \right\|$$

In the current paper, the horizontal converged RANS velocity is selected as the quantity for determining the optimal weights. Throughout the document, we use the notation $U_{x,M}$ to refer to the horizontal velocity corresponding to model M , \bar{U}_x for the high-fidelity counterpart, and U^{ref} (with the superscript "ref") to denote the reference velocity used for normalization (e.g., inlet velocity, velocity at the jet nozzle, etc).

The next step in the blending strategy consists in selecting and training a machine learning model to express the input/output relation between the features and the Gaussian model weights. To accomplish this, we first collect a diverse dataset of high-fidelity data, including experiments, DNS and LES data. The selected flows for training are described in Table 2. The training flows are then cross-simulated with each of the experts in the set \mathcal{M} . The modeled longitudinal velocities and their high-fidelity counterparts are then used to calculate the exact Gaussian weights for each model at the observation points locations. The flow physical features can then be estimated at these same points. Obviously, the expert models in \mathcal{M} do not predict the same flow features. In the non-intrusive space-dependent aggregation approach from [36], the features are assembled as a uniformly weighted average of those of the expert models, which mitigates the risk of overlooking flow patterns that are not captured by the baseline model. In the present work, we adopt the simpler choice of [37] and use the feature predicted by the baseline model. The argument for this choice is that the

expert data-driven models have been learned to correct the baseline in the training environments. Further studies of feature selection and estimation in prediction environments are warranted as future work.

Finally, given the baseline features and the exact weights at each observation location in the training set, we solve a machine learning regression problem of the form

$$\underbrace{\boldsymbol{\eta}(\mathbf{x}) = (\eta_1(\mathbf{x}), \dots, \eta_{11}(\mathbf{x}))}_{\text{baseline model local features}} \xrightarrow[\mathcal{W}]{\text{ML}} \underbrace{\{w_M(\mathbf{x})\}_{M \in \mathcal{M}}}_{\text{local model weights}} \quad (15)$$

where $\mathcal{W} : \boldsymbol{\eta} \rightarrow \{w_M\}_{M \in \mathcal{M}}$ is a highly nonlinear mapping to be determined. In the present study we approximate the features/weights mapping by means of a Random Forest Regressor (RFR), as previously done in [36, 37]. RFRs are particularly suited for this task due to their ability to capture complex, non-linear relationships, providing a robust and flexible predictive model. Alternative choices, such as Gaussian process regressors or neural networks could be also used (see [52] for a comparison of RFR and Gaussian process regressors).

Once the mapping \mathcal{W} has been learned, the RFR weighting functions are used to build the blended model corrections (13). The latter are finally propagated through the RANS solver to make predictions of the training flow cases or of new, unseen flows. The training and prediction workflows of the blending strategy are summarized through the Algorithms 1 and 2.

4 Numerical results

In this section, we investigate the performance of the blending model across a series of training and test flow cases.

After assessing the fidelity of the data-driven weighting functions, we propagate the blended model through the flow cases used to train the weights and the expert models, and verify that the blended model consistently assign higher weights to model trained for the considered flow topology. Subsequently, we demonstrate the generalization abilities of the proposed methodology by applying the trained blended model to unseen flow cases.

4.1 Flow solver

The data-driven models resulting from the SBL-SpaRTA algorithm are implemented within a modified version of the open-source finite-volume solver OpenFoam v23-06 [59]. In the numerical tests presented below, the governing equations are solved using SIMPLE algorithm. The linear upwinding is applied to the convective terms, while viscous terms are approximated with a second-order central difference scheme. The solution is advanced to the steady state by using a Gauss-Seidel smoother. For each case, we used the same computational settings and the same grids as in [21], to which we refer for more details. The grids are fine enough to ensure that the discretization error is negligible compared to the effect of the turbulence model.

Algorithm 1: Training of the features/weights mapping \mathcal{W} .

Input: Set of expert models \mathcal{M} , training HF flow data
Output: Trained RFR model \mathcal{W}

- 1 **Step 1: Simulations on training cases**
 for each training flow case (*e.g.*, turbulent channel, CD, CBFS, PH, ANSJ)
 do
 2 **for** each model $M \in \mathcal{M}$ **do**
 3 Run RANS to convergence using model M ;
 4 Extract streamwise velocity $U_{x,M}$;
 5 **end**
 6 **Step 2: Compute Gaussian weights**
 Using the modelled longitudinal velocity $\{U_{x,M}\}_{M \in \mathcal{M}}$ and its
 high-fidelity counterpart, evaluate the corresponding Gaussian weights
 $\{\omega_M\}_{M \in \mathcal{M}}$ at all observation points for the current training case;
 7 **Step 3: Extract the features**
 Evaluate local flow features $\boldsymbol{\eta}$ using the baseline model solution at all
 observation points;
 8 **end**
 9 **Step 4: Learn the mapping \mathcal{W}**
 Train the Random Forest to learn the mapping

$$\mathcal{W} : \boldsymbol{\eta} \rightarrow \{\omega_M\}_{M \in \mathcal{M}}$$

Save the learned model \mathcal{W} ;

4.2 Training of weighting functions

The feature-to-weight mapping \mathcal{W} is trained using the Random Forest Regressor (RFR) function from the `scikit-learn` Python library [60]. The RFR model has been configured with 100 estimators (trees) and a minimum of one sample per leaf. The quality of the splits is assessed using the squared error criterion. At each split, seven features were randomly selected, and a fixed random state has been employed to ensure reproducibility. The model has been trained on 80% of the dataset, while the remaining 20% is reserved for testing. The dataset includes all available observations of the horizontal velocity and the corresponding eleven physical features of [58], for all training cases. These cases include DNS data for a turbulent channel flow at $Re_\tau = 1000$ [61], PIV data for the ANSJ case [53], and LES or DNS data for the CBFS, CD, and PH cases (refer to Table 1 for reference). The specific mesh points from which the data were retrieved for each case are shown in Table 2.

The performance of the RFR model was evaluated using the R^2 criteria, which is commonly used to assess the predictive power of regression models. The R^2 score, also

Algorithm 2: Prediction of a flow scenario

Input: Flow scenario information; Trained RFR mapping \mathcal{W} .

Output: RANS blended-model solution

- 1 **Step 1:** Run RANS simulation using the baseline $k - \omega$ SST model.
 Step 2: Compute the set of local flow features $\boldsymbol{\eta}$ from the converged baseline solution.
- 2 **Step 3:** Use the trained RFR $\mathcal{W}(\boldsymbol{\eta})$ to predict local model weights at each prediction location, $\{w_M\}_{M \in \mathcal{M}}$.
- 3 **Step 4:** Assemble the blended RANS corrections b_{ij}^Δ and b_{ij}^R and use them to augment the baseline model $k-\omega$ SST

$$b_{ij}^\Delta = \sum_{M \in \mathcal{M}} w_M b_{ij}^{\Delta, M}, \quad b_{ij}^R = \sum_{M \in \mathcal{M}} w_M b_{ij}^{R, M};$$

- 4 **Step 5:** Solve the augmented RANS equations for the flow scenario until convergence
-

Case	Number of Data Points	Location of Points
ANSJ	1443	Subdomain: $(x/D_{jet}, y/D_{jet}) \in [1, 22] \times [0, 1.4]$
CD	14000	Total domain
CHAN	2400	Total domain
PH	15600	Total domain
CBFS	21000	Total domain

Table 2: Information on the training data used to learn the features/weights mapping by the RFR.

known as the coefficient of determination, is calculated as:

$$R^2 = 1 - \frac{\sum_{i=1}^N (y_i - \hat{y}_i)^2}{\sum_{i=1}^N (y_i - \bar{y})^2}$$

where y_i are the true values, \hat{y}_i are the predicted values, and \bar{y} is the mean of the true values. It measures how well the model fits the data by comparing the variance explained by the model to the total variance in the true values. For our application, the R^2 score for the training data was 0.991, indicating an excellent fit to the data the model was trained on. For the test data, the R^2 score was 0.99, demonstrating as well a strong predictive accuracy on unseen data by the RFR.

For a more detailed evaluation of the learned RFR performance, we investigate the distribution of the predicted weights versus the exact Gaussian weights, as shown in Fig. 1a. The scattered weights correspond to all models M_{ANSJ} , M_{SST} , and M_{SEP} . It can be seen that most of the training samples, representing 80% of the data, lie within a narrow band along the diagonal. This indicates that the RFR has successfully

captured the relationship between the flow physical features and the corresponding model weights for the training set. Furthermore, in Fig. 1b, we report the histogram depicting the discrepancies between the predicted and exact weights. All three weights are represented here as well. The histogram is strongly peaked at zero, suggesting that the deviations between the predicted and actual weights for the training set are minimal throughout. To further evaluate the generalization performance of the trained RFR, we examine the test set, representing the remaining 20% of the total data. In Fig. 1c, the scatter plot for the predicted versus exact weights for the test samples is shown. Similar to the training set, the test samples also follow the diagonal closely, and the distribution of discrepancies shown in Fig. 1d is strongly peaked at zero, indicating that the RFR has generalized well to the unseen test data. These results provide strong confidence in the robustness and accuracy of the trained RFR across both the training and validation data sets.

4.3 Application to the training flows

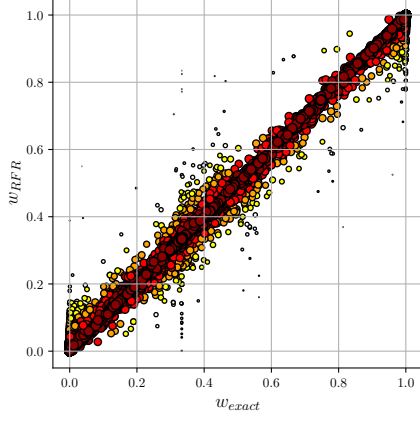
4.3.1 Turbulent Channel Flow $Re_\tau = 1000$

The first case considered in the training of the blending model is the turbulent channel flow at $Re_\tau = 1000$, where the baseline M_{SST} model is expected to perform optimally. The non-dimensionalized velocity profiles at $x = 0.97$ in Figure 2a show that as expected, the M_{SST} model aligns almost perfectly with ground truth data, requiring no significant adjustments. The accuracy of this model is further validated by its low mean absolute error (MAE) value, as shown in Table 3, and the absolute errors of the velocity profiles in Figure 2b, which reveals consistently minimal deviations across y^+ , especially in the log-law region. In contrast, while the M_{SEP} model provides a reasonable prediction, it exhibits a deviation from ground truth results, particularly noticeable in log-law region. The deviation is induced by the increase amount of eddy viscosity generated by the corrected model, which has been train to compensate the under-dissipative nature of the baseline model for strongly separated flows (see [23, 37]). The discrepancy is mirrored in the MAE values and error profiles, which, though higher than those of the M_{SST} model, still indicate acceptable performance. The M_{ANSJ} model, on the other hand, significantly overpredicts the flow velocity, and its error profiles reflect large discrepancies, particularly in the log-law region, showcasing its inadequacy for this flow scenario. In fact, the M_{ANSJ} correction tends to strongly reduce the eddy viscosity of the baseline model to compensate for the so-called jet anomaly [3]. However, the correction destroys the accuracy for attached wall-bounded flows.

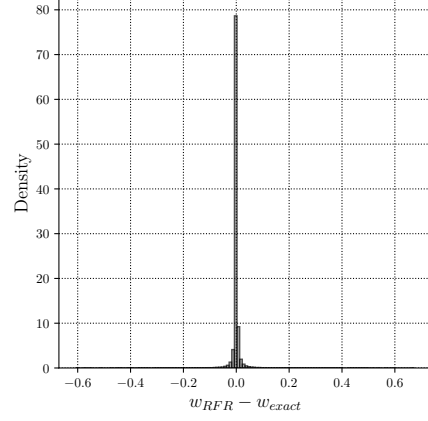
Of note, for this training flow case the blended model predominantly selects the baseline model, which is assigned a weight very close to one throughout the channel height. The contributions from the inaccurate M_{SEP} and M_{ANSJ} are effectively ruled out, according to their low performance scores.

4.3.2 Axis-symmetric near sonic jet flow

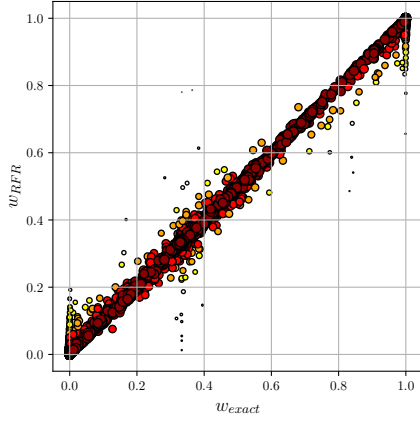
The axisymmetric near-sonic jet flow case, also used to train the expert model correction M_{ANSJ} , features a jet from the ARN2 nozzle with a radius of 1 inch and a jet exit



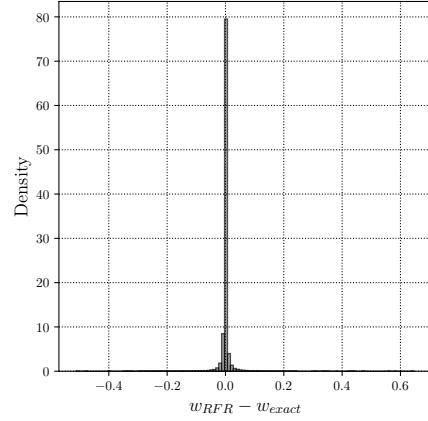
(a) Scatter plot of predicted vs. exact weights for the training set, representing 80% of the total data set.



(b) Error histogram for the discrepancies between predicted and exact weights for the training set.



(c) Scatter plot of predicted vs. exact weights for the test set, representing 20% of the total data set.



(d) Error histogram for the discrepancies between predicted and exact weights for the test set.

Fig. 1: Comparison of predicted weights versus exact weights using the Random Forest Regressor (RFR), and the distribution of prediction errors. The scatter plots highlight the accuracy of the predictions, and the histograms show the density of discrepancies between exact and predicted weights.

Mach number of $M_{jet} = 0.985$. This case involves complex flow phenomena near the jet exit, including turbulence interactions and potential shock-related effects, which are challenging to capture accurately with the baseline model.

As shown in Figure 3b, the expert M_{ANSJ} model provides as expected the most accurate velocity profiles at least in the far jet region, with a low mean absolute error

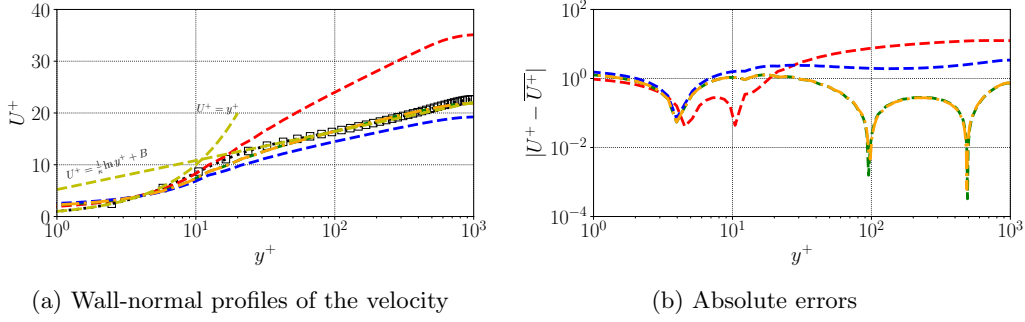


Fig. 2: Turbulent channel flow at $Re_\tau = 1000$. The legend denotes the following: ($\cdots \square \cdots$) DNS [61], ($---$) M_{ANSJ} , ($---$) M_{SST} , ($---$) M_{SEP} , ($---$) M_{blend} , and ($---$) theoretical prediction with the Kármán constants $\kappa = 0.41$ and $B = 5.2$.

	M_{ANSJ}	M_{SST}	M_{SEP}	Blended
$MAE(U^+)$	8.97	0.44	2.41	0.44

Table 3: Mean absolute error (MAE) for U^+ for the turbulent channel flow case $Re_\tau = 1000$.

(MAE) of 0.04 (Table 4). The M_{SST} model, underpredicts the velocity, resulting in a higher MAE of 0.09 (a known anomaly of most two-equation models), while the M_{SEP} model significantly underpredicts the velocity leading to the largest MAE of 0.16. These trends are confirmed by the absolute error profiles (Figure 3c) where M_{ANSJ} maintains the smallest errors, while M_{SEP} model exhibits the largest deviations throughout.

The blended model achieves an intermediate MAE of 0.07 which is close to that of the best performing model. As depicted in Figure 3d, the blending weights are initially distributed fairly equally among the models at the jet entrance, reflecting an effort to combine their contributions. As the flow develops through the shear layers, the relevance of M_{SEP} and M_{SST} decreases, leading to a reduction in their respective weights. Downstream of the jet, the M_{ANSJ} model becomes the dominant.

Further analysis of the velocity distribution along the jet axis (figure 4a) shows that the M_{ANSJ} model provides the closest match to the ground truth data, with M_{SST} underpredicting the velocity and M_{SEP} significantly underperforming. The blended model offers a reasonable compromise between the M_{ANSJ} and M_{SST} models, capturing the essential flow characteristics with relatively low errors (figure 4b). The weight distribution along the axis (figure 4c) further confirms the dynamic adjustment, with the M_{ANSJ} model taking over in regions where its performance is critical, while the other models contribute less further downstream.

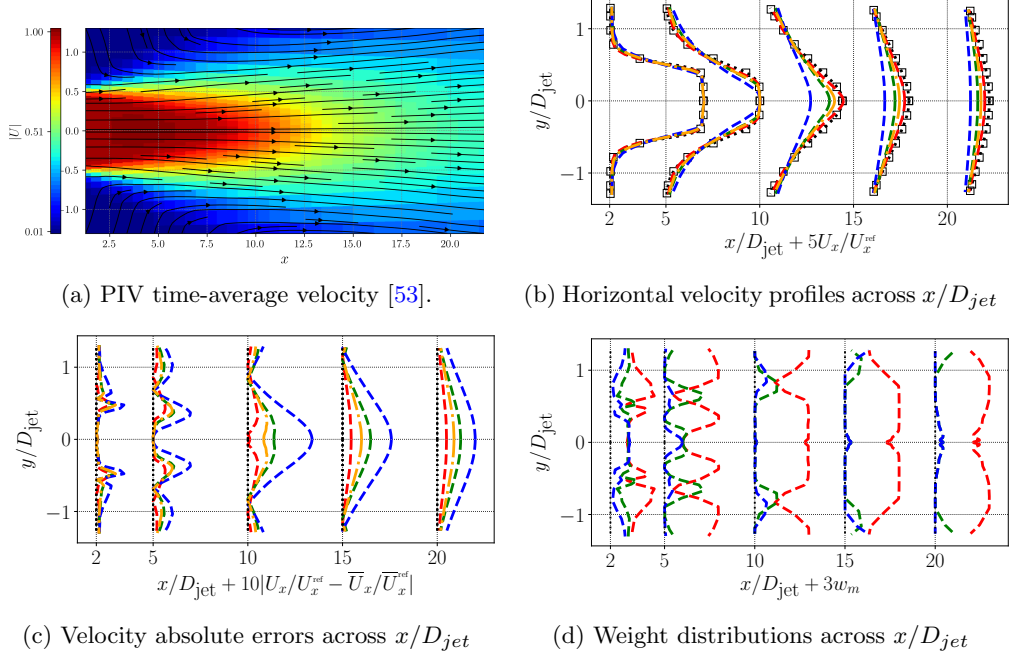


Fig. 3: Horizontal velocity, absolute errors and blending weights distributions for the axisymmetric near-sonic jet flow at stations $x/D_{jet} \in \{2, 5, 10, 15, 20\}$ with D_{jet} is the nozzle radius. The legend denotes the following: (.....□.....) PIV [53], (- - -) M_{ANSJ} , (- - -) M_{SST} , (- - -) M_{SEP} , (- - -) M_{blend} .

	M_{ANSJ}	M_{SST}	M_{SEP}	Blended
$MAE(U/U_{ref})$	0.04	0.09	0.16	0.07

Table 4: Mean absolute error (MAE) of the velocity in the near-sonic axisymmetric jet flow.

4.3.3 Separated Flow Cases

Hereafter, we present selected results from the separated flow training cases: the CD case, with a Reynolds number of $Re = 12600$, features flow over a converging-diverging channel; the PH case, with $Re = 10595$, involves turbulent flow over periodic hills; and the CBFS case, with $Re = 13700$, focuses on turbulent boundary layer separation over a curved ramp.

As expected, the M_{SEP} model consistently performs well across all the considered separated flow training cases, particularly in regions of separation and reattachment. The velocity profiles are in good agreement with the high fidelity data for the PH case (Fig. 5b) and the CBFS (not shown). However, the CD case is more challenging, because it is characterized by a small separation bubble in the divergent that cannot be captured by RANS model, even after data-driven correction. Nonetheless, the

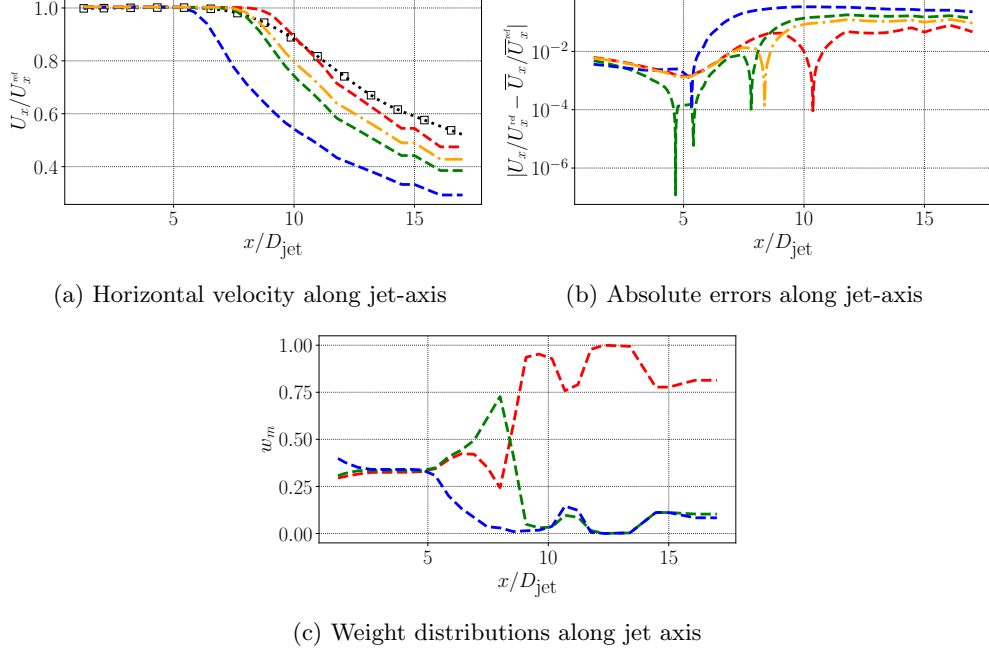


Fig. 4: Horizontal velocity, absolute errors and blending weights distribution along the jet axis. D_{jet} is the nozzle radius and the legend denotes the following: (..... \square) PIV [53], (---) M_{ANSJ} , (-.-) M_{SST} , (-.-) M_{SEP} , (-.-) M_{blend} .

M_{SEP} improves the baseline model (see Fig. 6b), even if the solution exhibits discrepancies with respect to the reference. On the contrary, the M_{ANSJ} model exhibits very poor performance for all the separated cases, for which it incorrectly predicts massive separation. The relative performance of the three expert models are better reflected in the error profiles, displayed in Figures 5c and 6c.

The blended model offers a fair performance across all separated flow cases. It effectively captures the flow dynamics in both attached and separated flow regions. This results in improved accuracy for the predicted velocity profiles with respect to the baseline model, especially in the separated regions. Inspection of the weight profiles (figures 5d and 6d) reveals that the M_{SEP} model is consistently assigned the highest weight, particularly in regions of strong separation, while the M_{SST} model is promoted in attached flow regions. The M_{ANSJ} model is always assigned low weights, reflecting its limited applicability in wall-bounded flow scenarios.

The blended model also improves significantly the predicted skin friction along the bottom wall, reported in Figure 7 for the three separated flow cases. The predominant contribution of M_{SEP} in separated regions, helps the blended model predicting strong separation and reattachment regions more effectively. On the other hand, M_{SST} is the main contributor in attached flow regions, thus ensuring better overall accuracy.

For a better quantification of the predictive accuracy of the various models, we report in Table 5 the mean absolute error (MAE) for all models and cases. It is noteworthy that, although the M_{SEP} model is more accurate than the other experts in separated regions, it can still lead to higher overall errors than the M_{SST} because of its lower performance in attached regions. On the other hand, the blended model consistently outperforms the individual models, showing that the feature/weight mapping effectively selects the most suitable experts according to the local flow physics.

MAE	M_{ANSJ}	M_{SST}	M_{SEP}	Blended
Periodic Hill (PH)				
U/U_{ref}	2.01	1.37	0.06	0.09
C_f	$3.53 \cdot 10^{-3}$	$2.37 \cdot 10^{-3}$	$2.65 \cdot 10^{-3}$	$2.07 \cdot 10^{-3}$
Converging-Diverging (CD) Channel				
U/U_{ref}	1.93	0.07	0.03	0.03
C_f	$4.31 \cdot 10^{-3}$	$2.83 \cdot 10^{-3}$	$2.61 \cdot 10^{-3}$	$2.15 \cdot 10^{-3}$
Curved Backward-Facing Step (CBFS)				
U/U_{ref}	0.03	0.01	0.02	0.01
C_f	$1.51 \cdot 10^{-3}$	$4.83 \cdot 10^{-4}$	$1.08 \cdot 10^{-3}$	$5.05 \cdot 10^{-4}$

Table 5: Mean absolute error (MAE) on the normalized streamwise velocity U/U_{ref} and the skin friction coefficient C_f for the PH, CD, and CBFS cases.

5 Application to unseen flows

In this section we evaluate the predictive performance of the blended data-driven model for two test cases selected from the NASA turbulence modeling testing challenge [6]. The first one is a simple zero-pressure-gradient boundary layer flow, at $M = 0.2$ and unit Reynolds number 5×10^6 , and is selected to check non-regression with respect to the baseline model for attached wall-bounded flows. The second one is the 2D NASA Wall-Mounted Hump (WMH) validation case involving a turbulent boundary layer separating over a smooth hump at a Reynolds number of $Re = 936\,000$, with a freestream velocity of $34.6 \text{ m} \cdot \text{s}^{-1}$. This case is characterized by flow acceleration, separation, reattachment and relaxation toward an equilibrium state.

5.1 Assessing training features coverage in the latent space

Prior to applying the blended model to unseen cases, we first analyze the distribution of the flow features used as input to the Random Forest Regressor (RFR) during training. The features $\boldsymbol{\eta}$ contain 11 physical features, each representing different aspects of the flow. To inspect the capability of the RFR model to generalize effectively to new, unseen cases, we reduce this 11-dimensional feature space into a two-dimensional latent space, with the latent variable denoted η . This dimensionality reduction helps visually assess whether the flow cases used for training adequately capture the variability of the

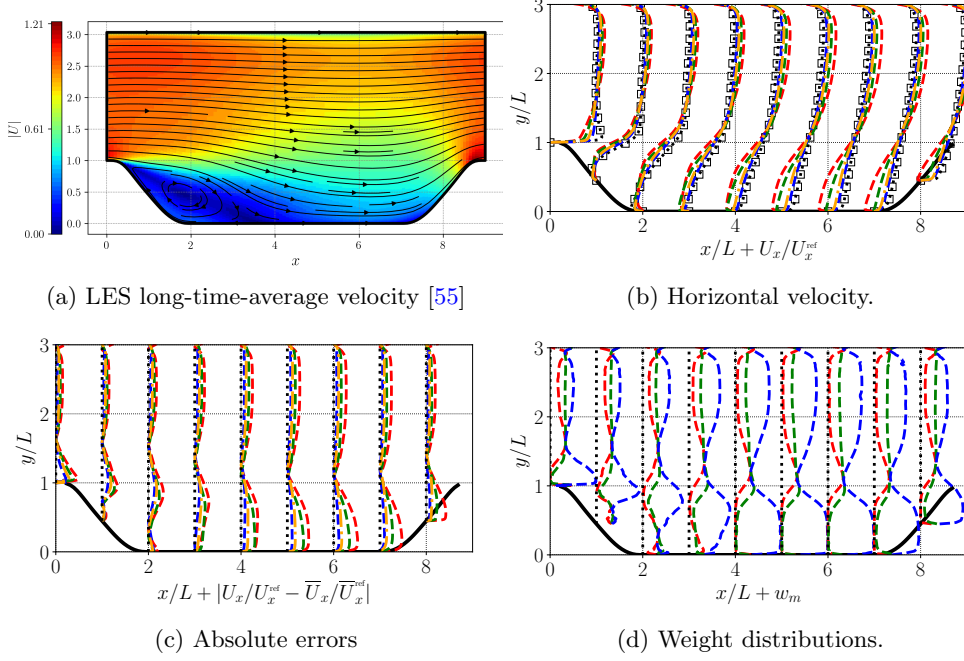


Fig. 5: Horizontal Velocity, absolute errors and blending weights for the PH case, at various stations $x/L \in \{0, 1, 2, 3, 4, 5, 6, 7, 8, 9\}$ with L the channel half-height (full channel height = $2L$). The legend denotes the following: ($\cdots\Box\cdots$) LES [55], ($---$) M_{ANSJ} , ($-.-$) M_{SST} , ($-\cdot-$) M_{SEP} , ($-\cdot-\cdot$) M_{blend} .

test cases. Before applying the dimensionality reduction techniques, we perform a pre-processing step using k -means clustering to reduce the density of data points in feature space. This is done to enhance the clarity of the subsequent analysis and allow for a more interpretable visualization of the latent structures. After clustering, we apply three dimensionality reduction techniques: PCA (Principal Component Analysis) [64], t-SNE (t-distributed Stochastic Neighbor Embedding) [65], and autoencoders [66, 67], to examine the distribution of features.

In the latent space, for the sake of clarity, we represent the spread and variance of the latent features using covariance regions, visualized as ellipses. These regions are constructed by calculating the covariance matrix of the latent variables η for each dataset, capturing how the data points are distributed in the two-dimensional space. The covariance matrix Σ is calculated as:

$$\Sigma = \frac{1}{N} \sum_{i=1}^N (\eta_i - \bar{\eta})(\eta_i - \bar{\eta})^T,$$

where N is the number of data points, η_i are the latent variables, and $\bar{\eta}$ is their mean. The covariance matrix describes the extent to which the latent variables co-vary

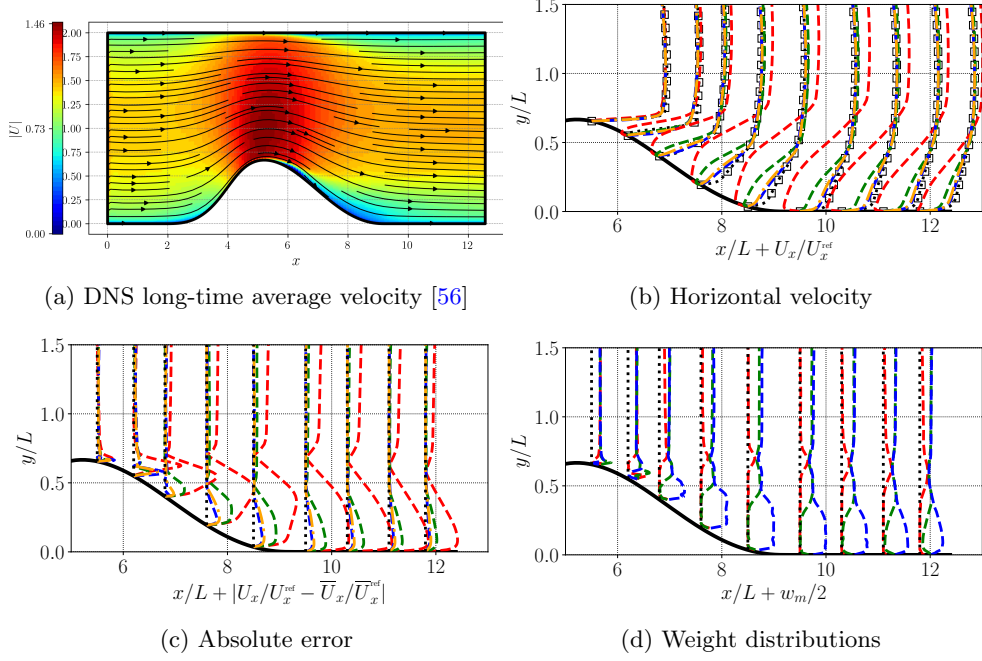


Fig. 6: Horizontal Velocity, absolute errors and blending weights for the CD case, at various stations $x/L \in \{5.5, 6.2, 6.8, 7.6, 8.5, 9.5, 10.3, 11.1, 11.8\}$ with L the channel half-height. The legend denotes the following: ($\cdots \square \cdots$) DNS [56], ($---$) M_{ANSJ} , ($---$) M_{SST} , ($---$) M_{SEP} , ($---$) M_{blend} .

with each other. From this, we compute the variance regions (represented visually as ellipses), where the axes are proportional to the eigenvalues λ_i of Σ . These regions show the spread of the data and represent the 95% confidence interval for the distribution of features, allowing us to assess how well the test cases are covered by the training data.

We begin by visualizing the data using PCA, which projects the data onto the directions of maximum variance. PCA primarily captures global structures, emphasizing large-scale relationships and variance within the dataset. As shown in Figure 8a, the training data for the different flow regimes generally covers the unseen cases well. However, the WMH test case displays broader variance compared to the training data, indicating a higher degree of variability. This suggests that while the training data captures the global variance effectively, some aspects of the test case’s variability may not be fully represented, likely due to PCA’s linear assumptions, which may overlook more complex, non-linear dependencies.

To investigate these non-linearities, we apply t-SNE, a non-linear dimensionality reduction method that prioritizes preserving local relationships between neighboring points. Unlike PCA, which emphasizes global variance, t-SNE focuses on maintaining local distances, making it particularly effective at revealing small-scale clusters and local structures. These local structures represent the relationships between points that

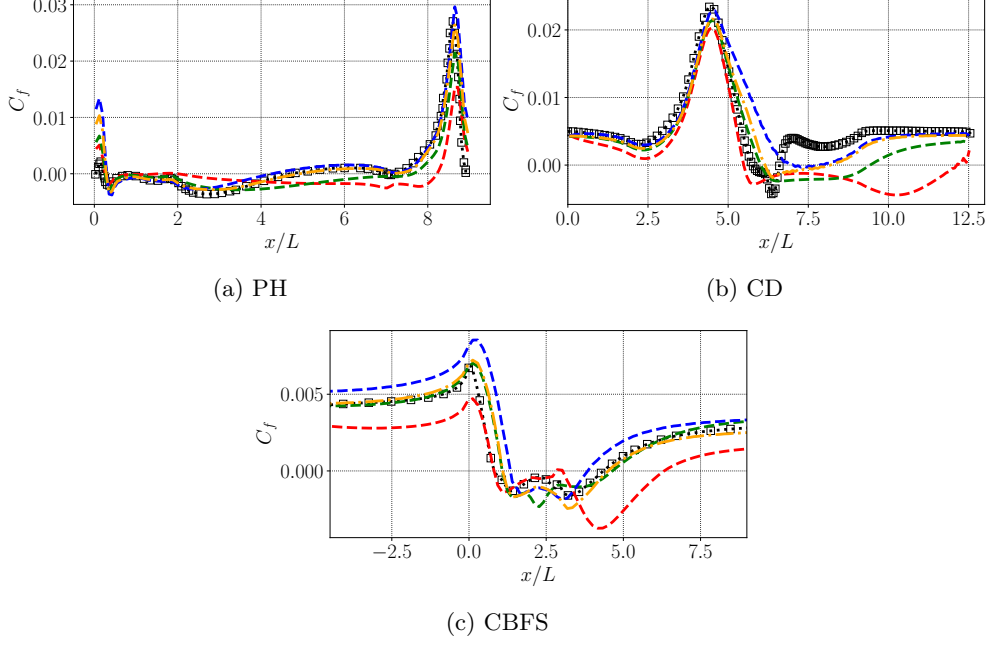


Fig. 7: Skin friction distributions along the bottom wall in the Periodic Hill (PH), Converging-Diverging channel (CD) and Curved Backward-Facing Step (CBFS) cases. L refers to channel half-height for CD, the step height for CBFS and hill height for PH. The legend denotes the following: (.....□.....) DNS for CD [56], LES for PH [62] and LES for CBFS [57, 63], (---) M_{ANSJ} , (- - -) M_{SST} , (- - -) M_{SEP} , (- - -) M_{blend} .

are close together in the high-dimensional space, which t-SNE preserves in the reduced space. We set the perplexity parameter to 30, which controls the number of nearest neighbors considered, balancing between local and global structure preservation. As shown in Figure 8b, the test cases are better represented within the training data distribution, with WMH being more closely aligned with the training data’s variance regions. Thus, t-SNE reveals that, when focusing on local relationships, the training data sufficiently spans the test cases in the latent space.

To gain a more comprehensive understanding of the latent space, we employ autoencoders. These models work by compressing the data into a lower-dimensional space and learning representations that allow for data reconstruction. This provides a balanced perspective, effectively capturing the non-linear dependencies preserving both local and global structures that might be missed by PCA or t-SNE. In our implementation, we take additional steps to regularize the latent space by constraining the latent variables within the unit ball. This normalization ensures stable training and reduces the likelihood of generating extreme representations. As shown in Figure 8c, the autoencoder captures the variance of both test cases (WMH and 2DZP) well within the variance regions of the training data, providing a clearer and more complete picture of the feature distribution.

In conclusion, the dimensionality reduction techniques, PCA, t-SNE, and autoencoders, offered different perspectives for inspecting how well the training data captures the test cases. While PCA offers an initial view focusing on global variance, t-SNE and autoencoders progressively improve our understanding of the alignment between the test and training data. Through this combined analysis of latent features, we have confirmed that the training data sufficiently represents the test cases, instilling confidence in the RFR model’s ability to generalize to unseen flow scenarios.

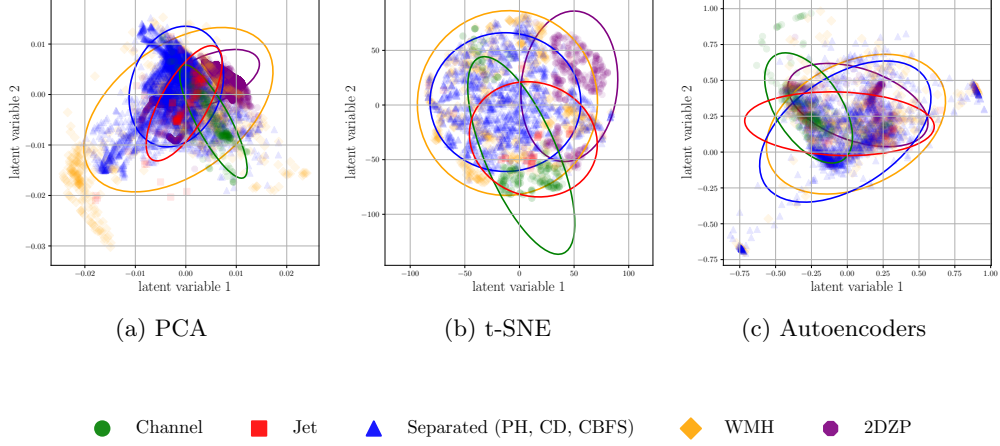


Fig. 8: Latent space projection of the physical flow features using PCA, t-SNE, and autoencoders. The ellipses represent variance regions based on the covariance matrix of the latent variables, with axes proportional to the square roots of the eigenvalues. These ellipses visualize the 95% confidence interval, indicating where the majority of the training data is concentrated.

5.1.1 2D Zero-pressure-gradient boundary layer flow

The first test case is the 2D Zero-pressure-gradient boundary layer flow. The velocity profiles normalized with respect to wall units at $x = 0.97$ are presented in Figure 9a. Similar to the training channel flow case, the M_{SST} model exhibits excellent agreement with the data from [68, 69] and theoretical predictions, supported by its low MAE, as shown in Table 6. The M_{SEP} model, while slightly under-predicting the velocity in the logarithmic region, still manages to capture the overall boundary layer trend reasonably well. In contrast, the M_{ANSJ} model significantly under-predicts the velocity across the entire boundary layer. In addition to Figure 9a, Figure 9b provides deeper insight into the behavior of the blended model. It shows that, while the blended model performs well, it does not quite reach the accuracy of the M_{SST} model in minimizing absolute errors for U^+ . However, the blended model still strikes a good balance, outperforming both the M_{SEP} and M_{ANSJ} models.

Regarding the blending behavior along y^+ , Figure 9c shows that, contrary to expectations, the M_{SST} model does not dominate the weight distribution along y^+ . Instead, the M_{ANSJ} model gains significant weight in the logarithmic region. This indicates that the shifts in model contributions in the log-law region have little impact on the overall accuracy, as all models ultimately yield similar corrections. Despite these variations, the blended model remains robust due to the balanced contributions from all models, ensuring consistent and reliable predictions across different regions of the boundary layer. When looking at the blending behavior along the wall (Figure 10b), we observe that the M_{SEP} and M_{SST} models dominate, with M_{SEP} contributing most strongly, followed by M_{SST} . Meanwhile, the M_{ANSJ} model has minimal influence along the wall.

This weights distribution allows the blended model to achieve a balanced prediction of C_f , resulting in the lowest MAE among all the models (Figure 10a and Table 6). In this case, the prediction of C_f illustrates the idea that selecting the best individual model is not always the optimal solution. Instead, it can be more advantageous to blend multiple models, leveraging their complementary strengths. By weighting different models appropriately, the blended approach achieves better overall performance, balancing both U^+ and C_f , and highlighting the versatility and robustness of the blended model.

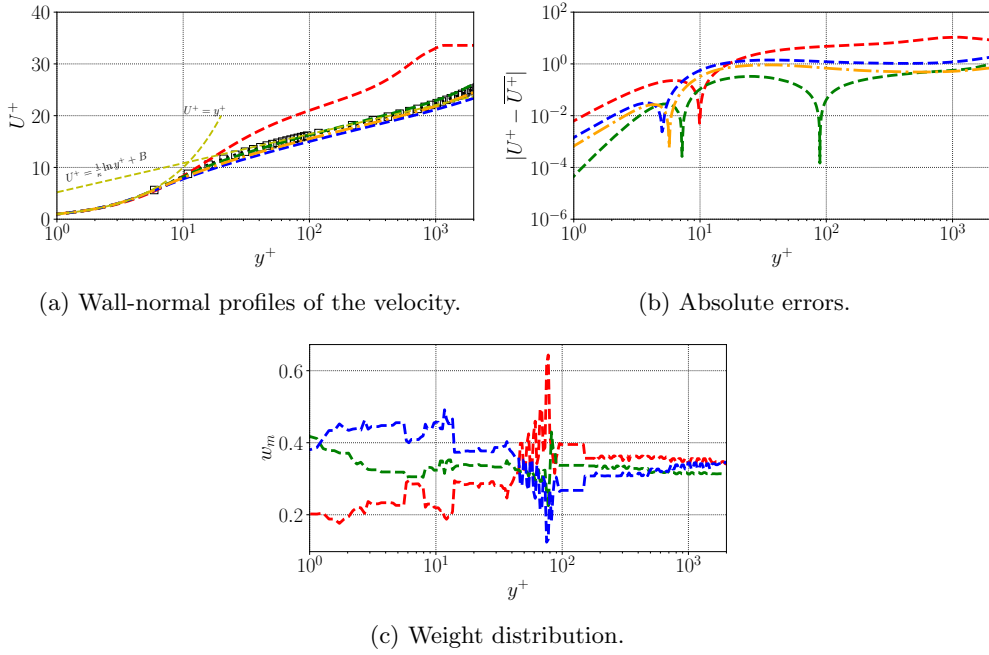


Fig. 9: 2D Zero-pressure-gradient boundary layer flow case. The legend denotes the following: (.....□.....) law-of-the-wall based on Coles' mean velocity profile [68, 69], (---) M_{ANSJ} , (---) M_{SST} , (---) M_{SEP} , (---) M_{blend} , and (---) theoretical prediction with the Kármán constants $\kappa = 0.41$ and $B = 5.2$.

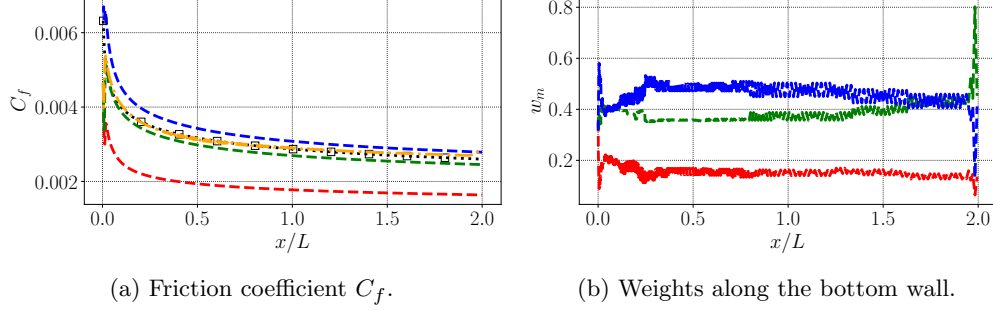


Fig. 10: Distribution of C_f for the 2D turbulent flat plate flow. L is the channel height and the legend denotes the following: ($\cdots \square \cdots$) White 6-121 [70], ($---$) M_{ANSJ} , ($---$) M_{SST} , ($---$) M_{SEP} , ($---$) M_{blend} .

	M_{ANSJ}	M_{SST}	M_{SEP}	Blended
$MAE(C_f)$	$1.15 \cdot 10^{-3}$	$1.75 \cdot 10^{-4}$	$2.60 \cdot 10^{-4}$	$5.66 \cdot 10^{-5}$
$MAE(U^+)$	6.28	0.41	1.47	0.72

Table 6: Mean Squared Error for C_f and U^+ , for the Turbulent Flat Plate flow.

5.1.2 Wall-Mounted Hump (WMH)

Our final test case is the turbulent flow through a channel with a wall-mounted hump. The velocity profiles and their respective absolute errors at various streamwise stations are presented in Figures 11b and 11c. For this case, the M_{SEP} model exhibits overall good performance compared to the other expert models. Specifically, it improves the representation of the velocity profiles in the separated region downstream of the hump with respect to the baseline model M_{SST} , although it predicts earlier reattachment than observed in the reference experimental data [71–73]. In contrast, the M_{ANSJ} model performs similarly to the training separated cases and largely overestimates the extent of the separation bubble.

The weight profiles (Figure 11d) show that M_{SST} and M_{SEP} are nearly equally weighted in the attached flow region upstream of the separation, while M_{SEP} takes precedence in the recirculation region and beyond. The M_{ANSJ} model, on the other hand, is assigned lower weights throughout both the attached boundary layer and the separated region. Interestingly, all weights tend to converge towards a value of $1/3$ in the core flow, indicating that this region is insensitive to the specific turbulence model used. The blended model’s solution closely mirrors that of M_{SEP} , with additional contributions from the other expert models helping to improve the prediction of the reattachment point.

The pressure and skin friction coefficient distributions along the bottom wall (Figures 12a and 12b) further highlight that the blended model strikes a compromise between the baseline M_{SST} , which overpredicts the extent of the separated region, and the M_{SEP} model, while minimizing the influence of the outlier M_{ANSJ} model, as evidenced by Figure 12c. The blended model's performance is further reflected in the distribution of weights along the bottom wall, where the M_{SEP} model dominates, followed by M_{SST} , contributing to a balanced and accurate prediction of the skin friction coefficient C_f . The M_{ANSJ} model has minimal influence in this region, reinforcing the reliability of the blended model's output.

In summary, the blended model performs well across the different quantities evaluated in this test case. It benefits from the strengths of each expert model, particularly M_{SEP} and M_{SST} , while effectively minimizing the errors contributed by M_{ANSJ} . This balanced behavior is evident in both the velocity profiles and skin friction distributions. The blended model achieves the lowest MAE for two out of the three metrics considered, as highlighted in Table 7, confirming its superior overall performance.

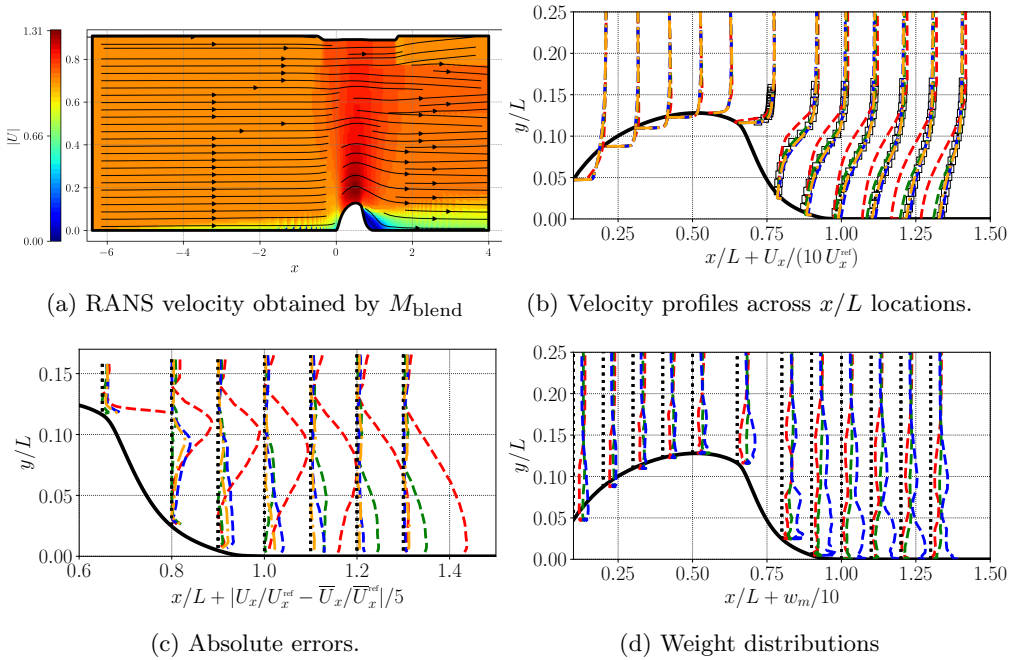


Fig. 11: Horizontal velocity, MAE and weighting functions at various streamwise stations of the WMH flow domain. L is the the bump "chord" and the legend denotes the following: ($\cdots \square \cdots$) experimental data [71, 72], ($---$) M_{ANSJ} , ($---$) M_{SST} , ($---$) M_{SEP} , ($---$) M_{blend} .

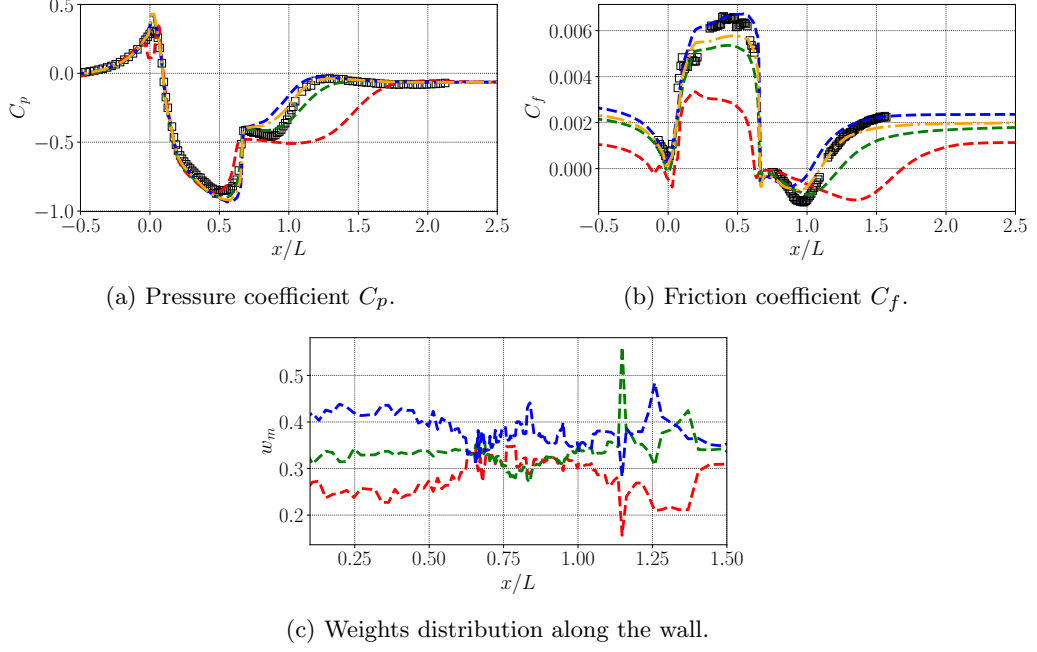


Fig. 12: Pressure coefficient and skin friction coefficient with the weights distributions along the bottom wall for the WMH flow case. L is the bump "chord" and the legend denotes the following: ($\cdots \square \cdots$) experimental data [73], ($---$) M_{ANSJ} , ($---$) M_{SST} , ($---$) M_{SEP} , ($---$) M_{blend} .

	M_{ANSJ}	M_{SST}	M_{SEP}	Blended
$MAE(U/U_{ref})$	0.24	0.06	0.06	0.04
$MAE(C_f)$	$2.17 \cdot 10^{-3}$	$7.53 \cdot 10^{-4}$	$4.21 \cdot 10^{-4}$	$3.86 \cdot 10^{-4}$
$MAE(C_p)$	0.09	0.03	0.05	0.04

Table 7: Mean squared errors on U , C_f , and C_p for the WMH flow.

6 Conclusion

This work introduced a novel machine learning-based methodology for blending expert data-driven models to improve the performance of the $k-\omega$ SST model across diverse flow configurations. The key feature of this approach is the internal blending mechanism within the RANS equations, which differs from existing non-intrusive blending methods [37]. This internal blending provides a unified solution by applying model corrections directly via weighting functions predicted by Random Forest Regressors (RFR), which are trained by using the solutions of the expert models.

The proposed blending approach operates in two distinct phases: an offline (learning) phase and an online (prediction) phase. During the offline phase, a mixture of available experts is selected, where each expert model is tailored to specialize in a

specific flow regime. Random Forest Regressors (RFR) are employed to dynamically adjust the contribution of each expert model based on local flow features. The available expert models used in this paper were trained across various flow regimes, including attached boundary layers, separated flows, and free-shear flows (such as axisymmetric jets). The flexibility of the weighting functions ensures that the most relevant expert models dominate in regions where they perform best, while less suitable models are downweighted. In the online phase, the computational process is streamlined into two steps. First, a baseline simulation is run to extract key flow features. Then, the blended correction is formed by using RFR and propagated within the RANS solver. To evaluate the effectiveness of the proposed methodology, the model was tested on several training and test flow cases from the NASA turbulence modeling testing challenge [6]. The test cases include both a 2D zero-pressure-gradient flat plate flow and the separated flow over a wall-mounted hump. The results demonstrate that the blended model outperforms the baseline M_{SST} model, particularly in challenging flow configurations where the baseline model struggles. In certain cases, the blended model even surpasses the best-performing individual expert models.

Looking ahead, future work should focus on refining the input features used to characterize the flow, as this could lead to even more accurate model predictions. Additionally, automatic clustering techniques could be employed to identify homogeneous data sets, allowing for more targeted expert model training [74]. Extending the methodology to more complex three-dimensional flows by incorporating additional expert models will be essential for validating the approach in more challenging configurations. Another important avenue for future work is exploring online training of the weighting functions and optimizing feature selection to better capture the flow characteristics. Addressing these challenges will enhance the accuracy and adaptability of the blended model, ensuring its robustness across a broader range of flow configurations.

Funding information

The authors gratefully acknowledge the support of Sorbonne University for providing the necessary resources and environment for this research.

A Input features

To incorporate information about the local flow physics, we selected a set of physical flow features among those initially introduced in [58], and summarized in 8. The latter are supplemented by an additional feature proposed in Ref. [75]:

$$\eta_{11} = \frac{P_k}{P_k + \epsilon}$$

which introduces information about turbulent flow regimes for which the baseline model $k - \omega$ SST delivers reliable predictions. Specifically, η_{11} is valuable in representing scenarios such as freely decaying turbulence, characterized by $P_k \rightarrow 0$ (hence, $\eta_{11} \rightarrow 0$), and equilibrium turbulence, where $P_k \approx \epsilon$, leading to $\eta_{11} \rightarrow \frac{1}{2}$.

Feature	Description	Formula	Feature	Description	Formula
η_1	Normalized Q criterion	$\frac{\ \mathbf{\Omega}\ ^2 - \ \mathbf{S}\ ^2}{\ \mathbf{\Omega}\ ^2 + \ \mathbf{S}\ ^2}$	η_6	Viscosity ratio	$\frac{\nu_T}{100\nu + \nu_T}$
η_2	Turbulence intensity	$\frac{k}{0.5U_i U_i + k}$	η_7	Ratio of pressure normal stresses to normal shear stresses	$\frac{\sqrt{\frac{\partial P}{\partial x_i} \frac{\partial P}{\partial x_i}}}{\sqrt{\frac{\partial P}{\partial x_j} \frac{\partial P}{\partial x_j} + 0.5\rho \frac{\partial U_k^2}{\partial x_k}}}$
η_3	Turbulent Reynolds number	$\min\left(\frac{\sqrt{k}\lambda}{50\nu}, 2\right)$	η_8	Non-orthogonality marker between velocity and its gradient [76]	$\frac{\left U_k U_l \frac{\partial U_k}{\partial x_l}\right }{\sqrt{U_n U_n U_i \frac{\partial U_i}{\partial x_j} U_m \frac{\partial U_m}{\partial x_j} + \left U_i U_j \frac{\partial U_i}{\partial x_j}\right }}$
η_4	Pressure gradient along streamline	$\frac{U_k \frac{\partial P}{\partial x_k}}{\sqrt{\frac{\partial P}{\partial x_j} \frac{\partial P}{\partial x_j} U_i U_i + \left U_l \frac{\partial P}{\partial x_l}\right }}$	η_9	Ratio of convection to production of k	$\frac{U_i \frac{\partial k}{\partial x_i}}{\left u'_j u'_j S_{ji}\right + U_l \frac{\partial k}{\partial x_l}}$
η_5	Ratio of turbulent time scale to mean strain time scale	$\frac{\ \mathbf{S}\ k}{\ \mathbf{S}\ k + \varepsilon}$	η_{10}	Ratio of total Reynolds stresses to normal Reynolds stresses	$\frac{\ u'_i u'_j\ }{k + \ u'_i u'_j\ }$

Table 8: List of input features used to train the weighting functions for the blended model.

B Constants and auxiliary relations for the k - ω SST

The constants of k - ω SST model are given bellow

$$\begin{aligned}
F_1 &= \tanh \left[\left(\min \left\{ \min \left[\max \left(\frac{\sqrt{k}}{\beta^* \omega y}, \frac{500\nu}{y^2 \omega} \right), \frac{4\alpha_\omega 2k}{CD_{k\omega}^+ y^2} \right]; 10 \right\} \right)^4 \right], \\
CD_{k\omega}^+ &= \max(CD_{k\omega}, 10^{-10}), \\
F_2 &= \tanh \left[\left(\min \left\{ \max \left(\frac{2\sqrt{k}}{\beta^* \omega y}, \frac{500\nu}{y^2 \omega} \right); 100 \right\} \right)^2 \right], \\
F_3 &= 1 - \tanh \left[\left(\min \left\{ 150 \frac{\nu}{\omega y^2}; 10 \right\} \right)^4 \right], \\
F_{23} &= F_2 F_3, \text{ if } F_3 \text{ is enabled, or } F_2 \text{ otherwise,} \\
D_k^{\text{Eff}} &= \nu + \alpha_k(F1)\nu_t, \\
D_\omega^{\text{Eff}} &= \nu + \alpha_\omega(F1)\nu_t
\end{aligned}$$

where y is blending function distance and $\alpha_k(F1)$, $\alpha_\omega(F1)$ are blending functions given by

$$\begin{aligned}
\alpha_k(F1) &= F_1 \alpha_{k_1} + (1 - F_1) \alpha_{k_2} \\
\alpha_\omega(F1) &= F_1 \alpha_{\omega_1} + (1 - F_1) \alpha_{\omega_2}
\end{aligned}$$

and

$$\begin{aligned}
\alpha_k &= (0.85, 1), \alpha_\omega = (0.5, 0.856), \\
\gamma &= (5/9, 0.44), \beta = (0.075, 0.0828).
\end{aligned}$$

$$\beta^* = 0.09, a_1 = 0.31, b_1 = 1, c_1 = 10$$

References

- [1] Spalart, P.: Strategies for turbulence modelling and simulations. *International Journal of Heat and Fluid Flow* **21**, 252–263 (2000)
- [2] Pope, S.B.: *Turbulent Flows*. Cambridge University Press, Cambridge, UK (2000)
- [3] Wilcox, D.C.: *Turbulence Modeling for CFD*, 3rd edn. DCW Industries, La Canada, California (2006)
- [4] P. Spalart: Philosophies and fallacies in turbulence modeling. *Progress in Aerospace Sciences* **74**, 1–15 (2015)
- [5] Durbin, P.A.: Some recent developments in turbulence closure modeling. *Annual Review of Fluid Mechanics* **50**, 77–103 (2018)
- [6] Rumsey, C., Coleman, G.: Nasa symposium on turbulence modeling: Roadblocks, and the potential for machine learning. Technical report (2022)
- [7] Schmitt, F.G.: About Boussinesq’s turbulent viscosity hypothesis: historical remarks and a direct evaluation of its validity. *Comptes Rendus Mécanique* **335**, 617–627 (2007)
- [8] Spalart, P., Shur, M.: On the sensitization of simple turbulence models to rotation and curvature. *Aerospace Science and Technology* **1**, 297–302 (1997)
- [9] Speziale, C.: On nonlinear k-l and k- ϵ models of turbulence. *Journal of Fluid Mechanics* **178**, 459–475 (1987)
- [10] Durbin, P.: Near-wall turbulence closure modelling without damping functions. *Theoretical and Computational Fluid Dynamics* **3**, 1–13 (1991)
- [11] Rodi, W.: A new algebraic relation for calculating the Reynolds stresses. *Gesellschaft Angewandte Mathematik und Mechanik Workshop Paris France* **56**, 219 (1976)
- [12] Pope, S.B.: A more general effective-viscosity hypothesis. *Journal of Fluid Mechanics* **72**(2), 331–340 (1975)
- [13] Gatski, T.B., Speziale, C.G.: On explicit algebraic stress models for complex turbulent flows. *Journal of Fluid Mechanics* **254**, 59–78 (1993)
- [14] Wallin, S., Johansson, A.V.: An explicit algebraic Reynolds stress model for incompressible and compressible turbulent flows. *Journal of Fluid Mechanics* **403**, 89–132 (2000)

- [15] Speziale, C.: A review of Reynolds Stress models for Turbulent shear flows. Technical Report NASA-CR-195054, NASA (1995)
- [16] Xiao, H., Cinnella, P.: Quantification of model uncertainty in RANS simulations: A review. *Progress in Aerospace Sciences* **108**, 1–31 (2019)
- [17] Duraisamy, K., Iaccarino, G., Xiao, H.: Turbulence modeling in the age of data. *Annual Review of Fluid Mechanics* **51**, 357–377 (2019)
- [18] Duraisamy, K.: Perspectives on machine learning-augmented Reynolds-Averaged and Large Eddy Simulation models of turbulence. *Physical Review Fluids* **6**, 050504 (2021)
- [19] Sandberg, R.D., Zhao, Y.: Machine-learning for turbulence and heat-flux model development: A review of challenges associated with distinct physical phenomena and progress to date. *International Journal of Heat and Fluid Flow* **95**, 108983 (2022)
- [20] Weatheritt, J., Sandberg, R.: A novel evolutionary algorithm applied to algebraic modifications of the RANS stress-strain relationship. *Journal of Computational Physics* **325**, 22–37 (2016)
- [21] Schmelzer, M., Dwight, R.P., Cinnella, P.: Discovery of algebraic Reynolds-stress models using sparse symbolic regression. *Flow, Turbulence and Combustion* **104**(2), 579–603 (2020)
- [22] Volpiani, P.S., Meyer, M., Franceschini, L., Dandois, J., Renac, F., Martin, E., Marquet, O., Sipp, D.: Machine learning-augmented turbulence modeling for RANS simulations of massively separated flows. *Physical Review Fluids* **6**(6), 064607 (2021)
- [23] Cherroud, S., Merle, X., Cinnella, P., Gloerfelt, X.: Sparse bayesian learning of explicit algebraic reynolds-stress models for turbulent separated flows. *International Journal of Heat and Fluid Flow* **98**, 109047 (2022)
- [24] Volpiani, P.S., Bernardini, R.F., Franceschini, L.: Neural network-based eddy-viscosity correction for RANS simulations of flows over bi-dimensional bumps. *International Journal of Heat and Fluid Flow* **97**, 109034 (2022)
- [25] Singh, A.P., Medida, S., Duraisamy, K.: Machine-learning-augmented predictive modeling of turbulent separated flows over airfoils. *AIAA journal* **55**(7), 2215–2227 (2017)
- [26] Holland, J.R., Baeder, J.D., Duraisamy, K.: Towards integrated field inversion and machine learning with embedded neural networks for RANS modeling. In: *AIAA Scitech 2019 Forum*, p. 1884 (2019)

- [27] Steiner, J., Dwight, R.P., Viré, A.: Data-driven RANS closures for wind turbine wakes under neutral conditions. *Computers & Fluids* **233**, 105213 (2022)
- [28] Amarloo, A., Cinnella, P., Iosifidis, A., Foroughi, P., Abkar, M.: Data-driven reynolds stress models based on the frozen treatment of reynolds stress tensor and reynolds force vector. *Physics of Fluids* **35**(7) (2023)
- [29] Wang, J.-X., Wu, J.-L., Xiao, H.: Physics-informed machine learning approach for reconstructing Reynolds stress modeling discrepancies based on dns data. *Physical Review Fluids* **2**(3), 034603 (2017)
- [30] Wu, J.-L., Xiao, H., Paterson, E.: Physics-informed machine learning approach for augmenting turbulence models: A comprehensive framework. *Physical Review Fluids* **3**(7), 074602 (2018)
- [31] Fang, Y., Zhao, Y., Waschkowski, F., Ooi, A.S., Sandberg, R.D.: Toward more general turbulence models via multicase computational-fluid-dynamics-driven training. *AIAA Journal* **61**(5), 2100–2115 (2023)
- [32] Bin, Y., Chen, L., Huang, G., Yang, X.I.: Progressive, extrapolative machine learning for near-wall turbulence modeling. *Physical Review Fluids* **7**(8), 084610 (2022)
- [33] Amarloo, A., Rincón, M.J., Reclari, M., Abkar, M.: Progressive augmentation of turbulence models for flow separation by multi-case computational fluid dynamics driven surrogate optimization. *Physics of Fluids* **35**(12) (2023)
- [34] Rincón, M.J., Amarloo, A., Reclari, M., Yang, X.I., Abkar, M.: Progressive augmentation of reynolds stress tensor models for secondary flow prediction by computational fluid dynamics driven surrogate optimisation. *International Journal of Heat and Fluid Flow* **104**, 109242 (2023)
- [35] Matai, R., Durbin, P.: Zonal eddy viscosity models based on machine learning. *Flow, Turbulence and Combustion* **103**, 93–109 (2019)
- [36] Zordo-Banliat, M., Dergham, G., Merle, X., Cinnella, P.: Space-dependent turbulence model aggregation using machine learning. *Journal of Computational Physics* **497**, 112628 (2024)
- [37] Cherroud, S., Merle, X., Cinnella, P., Gloerfelt, X.: Space-dependent aggregation of data-driven turbulence models. *arXiv preprint arXiv:2306.16996* (2023)
- [38] Lozano-Durán, A., Bae, H.J.: Machine learning building-block-flow wall model for large-eddy simulation. *Journal of Fluid Mechanics* **963**, 35 (2023)
- [39] Ho, J., Pepper, N., Dodwell, T.: Probabilistic machine learning to improve generalisation of data-driven turbulence modelling. *Computers & Fluids*, 106443

(2024)

- [40] Edeling, W.N., Cinnella, P., Dwight, R.P., Bijl, H.: Bayesian estimates of parameter variability in the k - ε turbulence model. *Journal of Computational Physics* **258**, 73–94 (2014)
- [41] Edeling, W.N., Cinnella, P., Dwight, R.P.: Predictive RANS simulations via Bayesian model-scenario averaging. *Journal of Computational Physics* **275**, 65–91 (2014)
- [42] Edeling, W.N., Schmelzer, M., Dwight, R.P., Cinnella, P.: Bayesian predictions of Reynolds-Averaged Navier-Stokes uncertainties using maximum a posteriori estimates. *AIAA Journal* **56**(5), 2018–2029 (2018)
- [43] Yuksel, S.E., Wilson, J.N., Gader, P.D.: Twenty Years of Mixture of Experts. *IEEE transactions on neural networks and learning systems* **23**(8), 1177–1193 (2012)
- [44] Jordan, M.I., Jacobs, R.A.: Hierarchical mixtures of experts and the EM algorithm. *Neural Computation* **6**(2), 181–214 (1994)
- [45] Hoeting, J.A., Madigan, D., Raftery, A.E., Volinsky, C.T.: Bayesian model averaging: a tutorial (with comments by m. clyde, david draper and ei george, and a rejoinder by the authors. *Statistical science* **14**(4), 382–417 (1999)
- [46] Menter, F.R.: Improved two-equation k - ω turbulence models for aerodynamic flows. Technical report (1992)
- [47] Weatheritt, J., Pichler, R., Sandberg, R.D., Laskowski, G., Michelassi, V.: Machine learning for turbulence model development using a high-fidelity hpt cascade simulation. In: *Turbo Expo: Power for Land, Sea, and Air*, vol. 50794, pp. 02–41015 (2017). American Society of Mechanical Engineers
- [48] Duraisamy, K.: Perspectives on machine learning-augmented reynolds-averaged and large eddy simulation models of turbulence. *Physical Review Fluids* **6**(5), 050504 (2021)
- [49] Saïdi, I.B.H., Schmelzer, M., Cinnella, P., Grasso, F.: CFD-driven symbolic identification of algebraic reynolds-stress models. *Journal of Computational Physics* **457**, 111037 (2022)
- [50] Stöcker, Y., Golla, C., Jain, R., Fröhlich, J., Cinnella, P.: Dns-based turbulent closures for sediment transport using symbolic regression. *Flow, Turbulence and Combustion* **112**(1), 217–241 (2024)
- [51] Tipping, M.E.: Sparse Bayesian learning and the relevance vector machine. *Journal of Machine Learning research* **1**, 211–244 (2001)

- [52] Cherroud, S.: Sparse bayesian learning and adaptative aggregation of data-driven turbulence models. PhD thesis, Arts et Métiers Institute of Technology (2023)
- [53] Bridges, J., Wernet, M.: Establishing consensus turbulence statistics for hot subsonic jets. In: 16th AIAA/CEAS Aeroacoustics Conference, p. 3751 (2010)
- [54] Breuer, M., Peller, N., Rapp, C., Manhart, M.: Flow over periodic hills—numerical and experimental study in a wide range of Reynolds numbers. *Computers & Fluids* **38**(2), 433–457 (2009)
- [55] Temmerman, L., Leschziner, M.A., Mellen, C.P., Frohlich, J.: Investigation of subgrid-scale models and wall-damping functions in large-eddy simulation of separated flow in a channel with streamwise periodic constrictions. *International Journal of Heat and Fluid Flow* **24**(2), 157–180 (2001)
- [56] Laval, J.-P., Marquillie, M.: Direct numerical simulations of converging–diverging channel flow. In: Kassinos, S.C., Lázaro, B.J., Reynard, G. (eds.) *Progress in Wall Turbulence: Understanding and Modeling*, pp. 203–209. Springer, Berlin, Germany (2011)
- [57] Bentaleb, Y., Lardeau, S., Leschziner, M.A.: Large-eddy simulation of turbulent boundary layer separation from a rounded step. *Journal of Turbulence* (13), 4 (2012)
- [58] Ling, J., Templeton, J.: Evaluation of machine learning algorithms for prediction of regions of high Reynolds-Averaged Navier-Stokes uncertainty. *Physics of Fluids* **27**(8), 085103 (2015)
- [59] OpenFOAM Foundation: Openfoam - the open source computational fluid dynamics toolbox (2023). Version 10
- [60] Pedregosa, F., Varoquaux, G., Gramfort, A., Michel, V., Thirion, B., Grisel, O., Blondel, M., Prettenhofer, P., Weiss, R., Dubourg, V., Vanderplas, J., Passos, A., Cournapeau, D., Brucher, M., Perrot, M., Duchesnay, E.: Scikit-learn: Machine learning in python. *Journal of Machine Learning Research* **12**, 2825–2830 (2011)
- [61] Lee, M., Moser, R.D.: Direct numerical simulation of turbulent channel flow up to $Re_\tau \approx 5200$. *Journal of Fluid Mechanics* **774**, 395–415 (2015)
- [62] Fröhlich, J., Mellen, C.P., Rodi, W., Temmerman, L., Leschziner, M.A.: Highly resolved large-eddy simulation of separated flow in a channel with streamwise periodic constrictions. *Journal of Fluid Mechanics* **526**, 19–66 (2005)
- [63] Lardeau, S., Leschziner, M.A.: The interaction of round synthetic jets with a turbulent boundary layer separating from a rounded ramp. *Journal of Fluid Mechanics* **683**, 172–211 (2011)

- [64] Sirovich, L.: Turbulence and the dynamics of coherent structures, parts i-iii. *Quarterly of Applied Mathematics* **45**, 561–590 (1987)
- [65] Maaten, L.v.d., Hinton, G.: Visualizing data using t-sne. *Journal of Machine Learning Research* **9**(Nov), 2579–2605 (2008)
- [66] Rumelhart, D.E., Hinton, G.E., Williams, R.J.: Learning internal representations by error propagation. In: Rumelhart, D.E., McClelland, J.L. (eds.) *Parallel Distributed Processing: Explorations in the Microstructure of Cognition*, Vol. 1: Foundations, pp. 318–362. MIT Press, Cambridge, MA (1986)
- [67] Hinton, G.E., Salakhutdinov, R.R.: Reducing the dimensionality of data with neural networks. *Science* **313**(5786), 504–507 (2006)
- [68] Coles, D.: The law of the wake in the turbulent boundary layer. *Journal of Fluid Mechanics* **1**(2), 191–226 (1956)
- [69] Bardina, J., Ferziger, J.H., Reynolds, W.C.: Turbulence modeling validation, testing, and development. Technical report, NASA Technical Memorandum 110446, Moffett Field, California (April 1997)
- [70] White, F.M.: *Viscous Fluid Flow*, 3rd edn. McGraw-Hill, New York (2006)
- [71] Greenblatt, D., Paschal, K.B., Yao, C.-S., Harris, J., Schaeffler, N.W., Washburn, A.E.: Experimental investigation of separation control part 1: baseline and steady suction. *AIAA journal* **44**(12), 2820–2830 (2006)
- [72] Greenblatt, D., Paschal, K.B., Yao, C.-S., Harris, J.: Experimental investigation of separation control part 2: zero mass-flux oscillatory blowing. *AIAA journal* **44**(12), 2831–2845 (2006)
- [73] Naughton, J.W., Viken, S., Greenblatt, D.: Skin friction measurements on the nasa hump model. *AIAA Journal* **44**(6), 1255–1265 (2006)
- [74] Roques, C., Dergham, G., Merle, X., Cinnella, P.: Non-intrusive space-dependent aggregation of updated RANS models via Bayesian calibration and machine learning. In: *IProceeding of the 4th International ERCOFTAC Symposium on Engineering Turbulence Modelling and Measurements* (2023)
- [75] Girimaji, S.: Machine learning, scale resolving simulations and the future of predictive computations of engineering flows: A perspective. In: *2022 Symposium on Turbulence Modeling: Roadblocks, and the Potential for Machine Learning* (2022)
- [76] Górlé, C., Iaccarino, G.: A framework for epistemic uncertainty quantification of turbulent scalar flux models for Reynolds-Averaged Navier-Stokes simulations. *Physics of Fluids* **25**(5), 055105 (2013)